

Prediction of irradiation induced microstructures in the AgCu model alloy using a multiscale method coupling atomistic and phase field modelling

G. Demange,^{1,*} L. Lunéville,² V. Pontikis,³ and D. Simeone¹

¹*DEN/DMN/SRMA/LA2M, CEA Saclay, 91191 Gif-sur-Yvette, France*

²*DEN/SERMA/LLPR, CEA Saclay, 91191 Gif sur Yvette, France*

³*DEN/DMN/LSI, CEA Saclay, 91191 Gif-sur-Yvette, France*

(Dated: September 11, 2022)

In this work, a multiscale approach based on phase field was developed to simulate the microstructure's evolution under irradiation in binary systems, from atomic to microstructural scale. For that purpose, an efficient numerical scheme was developed. In the case of AgCu alloy under Krypton ions irradiation, phenomenological parameters were computed using atomistic methods, as a function of the temperature and the irradiation flux. As a result, we predicted the influence of the irradiation flux and the temperature on the formation of patterned microstructures. In the case of AgCu, our model was qualitatively and quantitatively validated by a diffraction experimental study.

I. INTRODUCTION

Steady state patterned microstructures have lately sparked interest amidst the scientist community [1]. Such microstructures consist in predominance domains of bounded characteristic dimension. These domains can display a wide variety of morphologies, from labyrinthine patterns in polymer mixtures [2], to quasi-spherical Ni₃Al precipitates under ion irradiation [3]. The latter microstructure results from a ballistic disordering induced by the slowing down of impinging ions [4]. Recently, ion beam mixing process emerged as a proper candidate to manufacture patterned microstructures [5], for microelectronic industry notably [6]. The advantage of this fabrication process is the possibility to control microstructure features by such parameters as irradiation temperature and ion flux.

However, a quantitative description of the irradiation induced microstructure remains extremely challenging for two reasons. First, irradiated materials are brought very far from equilibrium, and their evolution cannot be described within the standard framework of statistical thermodynamics. Second, several time and space scales are involved in the process: starting from ballistic displacements induced by irradiation (10^{-12} s, 1 – 10 Å), passing by diffusion mechanisms (10^{-6}), up to precipitates growth (over years at millimetric scale). This is why, so far, this issue remains out of reach for atomistic approaches alone, such as Ab Initio methods and molecular dynamics [7, 8].

The present study aims at achieving greater understanding of materials microstructure far from equilibrium, where few analytical results can be found, at a relevant time and space scale. In the specific case of irradiated materials, it intends to classify the material microstructures by the mean of a phase diagram in the temperature-irradiation flux space, and more specif-

ically the temperature and flux leading to patterned microstructures in binary alloys.

This can only be achieved provided the number of freedom degrees are reduced, and space and time scales are crossed. The phase field method [9–11] meets these requirements. This approach has notably proved itself efficient to study aging in binary alloys [12]. Yet, it did not take irradiation effects into account in the first place. To overcome this limitation, Martin asserted that the thermal spike in a cascade could be taken into account by an athermal source term [13]. This idea was then invested by Bellon and al. [14]. Using a spectral approach, they could predict the formation of precipitates of stationary size due to ballistic effects, depending on reduced irradiation parameters [15]. Alternatively, a self-consistent method provided with greater accuracy in [16]. Yet, these studies were performed in adimensionalized coordinates, and no clear link to the temperature and the irradiation flux could be established, albeit Enrique and al. made a first attempt to overpass this limitation in [17]. Using a mixed molecular dynamics-kinetic Monte Carlo approach, they were able to demonstrate the possibility of disrupted coarsening for realistic temperatures and flux. However, their study remained also qualitative. Actually, so far, no complete scale jump, from atomic to microstructural scale, could be performed, in order to simulate the formation of patterned microstructure under irradiation. In particular, no computation of the patterning domain in the temperature-flux plane was achieved.

In this work, the phase field method was developed to simulate the microstructure's evolution under irradiation in binary systems, at the relevant time and space scales. For that purpose, a new phase field model taking irradiation effects into account was set and physically justified. An efficient numerical scheme was developed to simulate the long stage microstructure in reduced units. Atomistic methods were implemented to compute the phenomenological parameters, as a function of temperature and irradiation flux, for the AgCu model alloy under Krypton ions irradiation. The different microstructures of ion irradiated alloys were classified in a temperature-flux out of

* gilles.demange@univ-rouen.fr

equilibrium *phase diagram*. This diagram was eventually qualitatively and quantitatively validated by a diffraction experimental study [18]. The choice of the AgCu system was first motivated by the presence of a large miscibility gap for temperatures inferior to the critical temperature. Besides, AgCu, Ag, and Cu crystals are invariant under the same space group $Fm\bar{3}m$. As such, the silver-copper alloy undergoes an isostructural phase transition when the binodal is crossed. This system can hence be characterized by the scalar concentration of one of its components. From a practical standpoint, this system comes with numerous experimental data on the thermodynamic properties of its components and the alloy, as well as various numerical studies to compare with, notably in [17]. In particular, the strong contrast factor between copper and silver makes this alloy compatible with diffraction measures. For all these reasons, AgCu is a convenient application system.

This work is structured as follows. First, the phase field model, where a ballistic term and dependence of atomic mobility on irradiation flux was added, is presented. Second, the numerical methods at use are detailed. Then, results are displayed in the following order. The phenomenological parameters in the phase field model are estimated for AgCu under Krypton ions irradiation. Then, the phase diagram of the irradiated system provided by our numerical phase field approach in reduced coordinates is displayed. Finally, this diagram is expressed in the flux-temperature plane, and comparison with a diffraction study from the literature is discussed.

II. PHASE FIELD MODEL WITH A BALLISTIC CONTRIBUTION

1. Equilibrium model

Within the phase field model [19], the microstructure of binary alloys can be characterized by the coarse grained concentration $c(\mathbf{r}, t)$ of one component. In the case of phase separation, the evolution of the concentration can be modelled using the Model B equation [11]:

$$\frac{\partial c}{\partial t} = \bar{M} \nabla^2 \left[\frac{\delta F}{\delta c}(c) \right], \quad (1)$$

where \bar{M} is the atomic mobility, and $F(c)$ is the free energy. Equation Eq. (1) describes the system evolution from a non equilibrium state to equilibrium, through minimisation of its free energy, via diffusional mechanisms. For a heterogeneous system, F can be written [9]:

$$F(c) = \int_{\Omega} \left[f_h(c) + \frac{\kappa}{2} |\nabla c|^2 \right] d\Omega. \quad (2)$$

Here, $f_h(c)$ is the homogeneous free energy density, and $\kappa |\nabla c|^2 / 2$ is the energy cost of diffuse interface formation

in a heterogeneous medium. $\kappa > 0$ is the stiffness parameter, which is proportional to the interface energy. Based on Lifshitz's criterion for the small fluctuations of the concentration from their concentration in liquid state c_L , f_h can be expanded in Taylor series with respect to the concentration deviation $c - c_L$:

$$f_h(c) = \frac{a_2(T)}{2}(c - c_L)^2 + \frac{a_3(T)}{3}(c - c_L)^3 + \frac{a_4(T)}{4}(c - c_L)^4. \quad (3)$$

Contrary to the standard Cahn-Hilliard equation [10], a cubic term was added to f_h , so that first order phase transitions could be accounted for [20]. In particular, this term will be required in the case of AgCu. f_h displays two minima corresponding to two stable equilibrium states. These minima are defined by Hazewinkel's approach for stationary solutions of Eq. (1), in the case of non symmetric potentials [21]. At equilibrium, c_+ and c_- satisfy $f'_h(c_+) = f'_h(c_-)$, $f''_h(c_+) = f''_h(c_-)$ and $f''_h(c_{\pm}) > 0$, where function f_h is derived with respect to the concentration. The last condition ensures the stability of both phases at equilibrium. This provides with:

$$c_{\pm} = -\frac{a_3}{3a_4} \pm \sqrt{\frac{1}{3} \left(\frac{a_3}{a_4} \right)^2 - \frac{a_2}{a_4} + c_L}. \quad (4)$$

In Eq. (1), the atomic mobility \bar{M} plays a dominant part in the definition of the time scale of the dynamics. It was determined in Onsager's formalism [22], under Darken's approximation [23]. As is, this led M to depend strongly on c , through the factor $c(1 - c)$ (see appendix B). This factor actually restrains diffusion to interfaces only, as $c(1 - c) \rightarrow 0$ far from interfaces. This corresponds to interface diffusion, characterized by a $t^{1/4}$ growth law of precipitates [24]. However, experiments observed a $t^{1/3}$ growth law [25], associated to bulk diffusion. The $c(1 - c)$ factor was hence averaged, so that Martin's standard expression for \bar{M} [26] was recovered:

$$\bar{M} = \frac{\bar{c}(1 - \bar{c})}{k_B T} \tilde{D}. \quad (5)$$

Here, \bar{c} is the mean concentration, and \tilde{D} is the chemical interdiffusion coefficient [22]. \tilde{D} theoretically depends on $c(\mathbf{r}, t)$ as well. Yet, in the case of similar isotopic diffusion coefficients of both species in the alloy [27], it can be approximated by an average isotopic diffusion coefficient, thus independent of c [28]. This assumption will be satisfied by the AgCu alloy, due to very close creation and migration energies [29–33].

2. Irradiation effects

In our study, we made the assumption that irradiation impacted the microstructure of an alloy through two

main mechanisms: ballistic effects induced by atomic relocations, and diffusion enhancement due to point defects recreation.

As for ballistic effects, Martin suggested that they could be described by an athermal term [13]. The local fluctuations of concentration induced by irradiation could then be expressed by a local matter balance [34]:

$$\frac{\partial c}{\partial t} = \Gamma \times (p_R * c - c). \quad (6)$$

Here, Γ is an atomic relocation frequency, and p_R a probability distribution of displacements in subcascades. It involves Sigmund and Gras Marti ion mixing formalism [35]. Ion mixing asserts that ballistic effects can be treated as an homogeneous source term. The justification relates to the strong gap of time scale between the ballistic stage of a displacements cascade (~ 100 ps), and precipitates growth driven by diffusion (~ 1 ms). The evolution of the microstructure under irradiation is thus the result of two mechanisms, acting separately on two different time scales. This assumption withal requires that the covering volume fraction of the cascade by subcascades, f_r , exceeds the percolation threshold [36]:

$$f_r = n_{sc} \times \frac{l_{sc}}{L_c} \geq 0.2. \quad (7)$$

Here, n_{sc} , l_{sc} and L_c are the number of subcascades within the cascade, the width of the cascade and its length respectively. This makes the microstructure only sensible to the average effect of numerous cascades covering one another. The strong heterogeneity due to subcascades [37] can hence be passed over, and every point \mathbf{r} in the henceforth homogeneous cascade can be considered as the center of a subcascade. Therefore, p_R does not depend on the position, but on the flight distance r between the initial and final position of the displaced atom only. We assumed that p_R followed an exponential decay, mimicking small displacements in subcascades:

$$p_R(r) = \frac{1}{2\pi R^2} \exp\left(\frac{-r}{R}\right). \quad (8)$$

Here R is the mean relocation distance. As for Γ , it is the product of the irradiation flux Φ , and a relocation macroscopic cross section σ^d :

$$\Gamma = \sigma^d \Phi, \quad \sigma^d = \frac{V_{cell}}{N_{cell}} \times \frac{N_d}{L_c}. \quad (9)$$

Here, V_{cell} and N_{cell} are the cell volume and number of atoms per cell. N_d is the number of relocated atoms per cascade.

The second phenomenon related to irradiation is the enhancement of atomic diffusion, due to point defects

recreation. Introducing additional vacancies and interstitials concentration δc_V^{irr} and δc_I^{irr} , the irradiation contribution M^{irr} to the mobility can be written [38]:

$$M^{\text{irr}} = \frac{\bar{c}(1-\bar{c})}{k_B T} [\delta c_V^{\text{irr}} D_V + \delta c_I^{\text{irr}} D_I], \quad (10)$$

where D_V and D_I are the vacancy and interstitial diffusion coefficients in the alloy. This expression requires that D_V and D_I are very close for each species of the alloy [28]. This assumption will once again be satisfied in the case of AgCu system. The values of δc_V^{irr} and δc_I^{irr} were estimated by the chemical model of Sizmann [38]. Thermal recombination, and sink absorption at interfaces were also taken into account [39]. As point defects migration takes place on a very small time scale ($\sim 10^{-9}$ s) in comparison with precipitates growth ($\sim 10^{-6}$ s), their concentration can be set at their equilibrium value. It is defined by the final state of Sizmann's equations (see appendix B). The total mobility M then reads:

$$M = \bar{M} + M^{\text{irr}}. \quad (11)$$

In this case, M depends on both temperature and irradiation flux. Its expression is given in appendix B. Finally introducing ballistic term of Eq. (6) in Eq. (1), the Cahn-Hilliard equation under irradiation becomes:

$$\frac{\partial c}{\partial t} = M \nabla^2 [f'_h(c) - \kappa \nabla^2 c] + \Gamma(p_R * c - c). \quad (12)$$

Let us remark that in the phase field model, atomic fluctuations were passed over by the coarse graining procedure. Strictly speaking, they should be accounted for by the *ad-hoc* introduction of a noise, consistently with Cook's approach [40]. However, this study focuses on low temperatures, where noise effects upon the microstructure are small. They were hence neglected in this work.

3. Adimensionalized equation and space and time scales

To model the microstructural evolution in an irradiated material, the phase field equations were rewritten in their reduced form first. The reduced concentration ϕ is defined from the solubility limits c_{\pm} displayed in Eq. (4), so as to vary between -1 and $+1$ in the absence of irradiation and without asymmetry in the free energy:

$$\phi = \frac{c - c_L}{\alpha}, \quad \text{where} \quad \alpha = \frac{c_+ - c_-}{2}. \quad (13)$$

Using Eq. (12), the evolution of ϕ is given by the equation:

$$\frac{\partial \phi}{\partial t'} = \nabla^2 [[3\lambda^2 - 1]\phi - 3\lambda\phi^2 + \phi^3 - \nabla^2 \phi] + W(p_R * \phi - \phi). \quad (14)$$

This procedure reduces the number of parameters from 6 ($a_2, a_3, a_4, \Gamma, R, M$) to 3 (λ, W and R'), without loss of information. These 3 reduced parameters are linked to the 6 original ones, through the phase field time and space scales t_0 and l_0 :

$$\begin{cases} t_0 = \frac{|a_2|\xi^2}{Ma_4^2\alpha^4V_{\text{at}}}, & l_0 = \frac{1}{\alpha}\sqrt{\frac{\kappa}{a_4}}, \quad t' = \frac{t}{t_0}, \quad \mathbf{r}' = \frac{\mathbf{r}}{l_0}, \\ W = t_0\Gamma, \quad R' = \frac{R}{l_0}, \quad \lambda = \frac{c_+ + c_- - 2c_L}{c_+ - c_-}. \end{cases} \quad (15)$$

Here, V_{at} is the mean atomic volume of the alloy's species. λ can be seen as the reduced asymmetry parameter of the 2:3:4 potential f_h in Eq. (3). R' is the atomic displacement range ratio between ballistic relocations and diffusion. Finally, W is the reduced intensity of ballistic effects. It yields the frequency of ballistic relocations Γ , and diffusion migration M . Prime notations are dropped in the following, except for R' , as both R and R' will be used.

Finally, Eq. (14) was not the most suitable form for the elaboration of a phase field numerical scheme. For that purpose, it was rewritten under variational form:

$$\begin{cases} \frac{\partial\phi}{\partial t} = \nabla^2 \left[\frac{\delta\mathcal{L}}{\delta\phi}(\phi) \right], \\ \mathcal{L}(\phi) \equiv F(\phi) + \frac{W}{2} \int_{\Omega} \{g * \phi\}(\mathbf{r}, t) \phi(\mathbf{r}, t) d\mathbf{r}, \end{cases} \quad (16)$$

where as $-\nabla^2 g = \delta - p_R$. The insight of Eq. (16) is to interpret the dynamics of the system, as the minimization of an effective energy for the irradiated system, as $\mathcal{L}(\phi)$ is a strict Lyapunov function. Stationary states can thereupon be seen as minima of \mathcal{L} [41].

III. SIMULATION METHOD

A. Parameters simulation

1. Equilibrium parameters

Coefficients a_2, a_3 and a_4 , defining the free energy density $f_h(c)$ in Eq. (3), were estimated using the experimental AgCu phase diagram from [42]. Indeed, Eq. (4) links these parameters to the experimental solubility limits c_{\pm} , for a given temperature T . Yet, Eq. (4) only provides with two relations, which is insufficient to compute three parameters. A third constraint should thus be set. This was given by an additional assumption on the factorization of $f_h(c)$. By construction, $f_h(c)$ was divided in a symmetric part $\omega(c)$, this is the grand-canonical potential density, and an asymmetric contribution $\Delta\mu c/V_{\text{at}}$, corresponding to the chemical potential gap between atomic species. In the case of AgCu, $\Delta\mu = -0.44$ eV between silver and copper [43], and

$V_{\text{at}} = 13.4 \text{ \AA}^3$. The factorization assumption was made on $\omega(c)$, namely $\omega(c) = D(c - c_+)^2(c - c_-)^2$. This way, $\omega(c)$ was minimized by the solubility limits satisfying $\omega'(c_+) = \omega'(c_-) = 0$, and both wells of $\omega(c)$ had the same depth $\omega(c_+) = \omega(c_-)$. This provided with $f_h(c) = D(c - c_+)^2(c - c_-)^2 + \Delta\mu c/V_{\text{at}}$, and consequently a_2, a_3 and a_4 .

The interface profile and the stiffness parameter κ were determined using a mixed molecular dynamics-Monte Carlo approach, for $T = 600, 700, 800$ and 900 K. The interatomic potential computed by Briki [43] was chosen, as it led to a correct phase diagram for AgCu. The simulation sample was made of a silver and a copper block, stuck in the $\langle 100 \rangle$ direction, for a total of 11700 atoms. The tangential constraint due to the misfit between Ag and Cu cell parameter ($\sim 13\%$ [44]) was geometrically minimized with a 8/9 ratio for the number of atomic rows between silver and copper. The relaxation of the remaining tangential constraint was performed using a MD simulation at 0 K, using the Verlet algorithm with time step $\Delta t = 10^{-15}$ s. Computations were speeded up with the simulated annealing method. Starting from this state, the equilibrium interdiffusion concentration profile of silver at the interface between blocks was determined using a Monte Carlo method in the pseudo grand canonical ensemble. The displacement proposal in the Markov chain included atomic species switch to mimic interdiffusion at the interface, as well as thermal and elastic relaxation. The acceptance-reject probability was computed using the Gibbs potential derived from the same interatomic potential as in the previous step, and $\Delta\mu = 0.44$ eV [43]. Afterwards, these profiles were fitted with a Jacobi elliptic sine function [45]. The fit was performed with respect to both κ and the form coefficient of the elliptic sine, governing the nature of the interface. It eventually provided with $\kappa(T)$ (see appendix A).

It should be noted that κ was determined in the $\langle 100 \rangle$ direction only, and $\langle 110 \rangle$ and $\langle 111 \rangle$ directions were passed over. The absence of the $\langle 110 \rangle$ direction can be easily justified by the fact it is not an equilibrium surface of the crystal, contrary to $\langle 100 \rangle$ and $\langle 111 \rangle$ directions. Besides, the $\langle 111 \rangle$ surface displays the smallest energy, and $\langle 100 \rangle$ could hence be considered as the surface representing for high energy interfaces, when no elastic contribution is introduced.

2. Displacement cascade simulation

Displacement cascades were simulated using the Binary Collision Approximation code MARLOWE. This provided with the ballistic relocation frequency Γ , the mean relocation range R , and the irradiation enhanced mobility M . Contrary to MD simulations, MARLOWE is capable of simulating high energy incident ions irradiation required to achieve microstructure patterning [8, 46]. Besides, it accounts for crystal structure and associated atomic effects, such as channelling and replacement se-

quences. This explains why MARLOWE's simulations often match molecular dynamics [47], yet requiring less computation time [48]. The nuclear stopping power was the standard Molière potential, and the electronic stopping potential was taken from SRIM semi-empirical inelastic potential [49]. Simulations were performed on homogeneous polycrystalline Ag₅₀Cu₅₀ subjected to 1 MeV Krypton incident ions in orthogonal incidence.

B. Phase field simulations

Phase field simulations on Eq. (12) were performed in two dimensions using a finite difference scheme in time, coupled with a spectral treatment of space. The phase field numerical scheme was elaborated to solve Eq. (14) for long simulation times, where potential stationary states are reached. Eq. (14) involves fourth order space derivatives. This leads to an overconstraining stability condition on the time step Δt , if treated explicitly. For that purpose, we chose to adapt Eyre's semi implicit time scheme [50, 51], for time dependent gradient systems [52] to our equation. It profits with the possibility to write Eq. (14) under variational form in Eq. (16). Following Eyre's algorithm, $\mathcal{L}(\phi)$ was split into a contracting and an expansive part. The first one was treated implicitly, in order to allow the time scheme to inherit with this flow-contracting property. The second one was treated explicitly. The splitting between explicit and implicit term was linear, so that the time scheme was compatible with a spectral treatment of space. The resulting scheme was unconditionally gradient stable, as it inherited [52] with the global Lyapunov stability of the continuous solutions [53]. This choice led to a first order in time.

Besides, we chose the Fourier collocation treatment of space [54]. This choice allowed to get rid of spatial derivatives, thus achieving faster computation. It lead to an infinite convergence order in space. The final scheme for each \mathbf{k} mode of the discrete solution in Fourier space after n iterations ($\hat{\phi}_{\mathbf{k}}^n$) reads:

$$\hat{\phi}_{\mathbf{k}}^{n+1} = \frac{1}{1 - \Delta t \rho(\mathbf{k})} \left(\hat{\phi}_{\mathbf{k}}^n + \Delta t \left\{ a_{\mathbf{k}} \left[\hat{\phi}_{\mathbf{k}}^n \right] - \rho(\mathbf{k}) \hat{\phi}_{\mathbf{k}}^n \right\} \right), \quad (17)$$

where factors $a_{\mathbf{k}}$ and $\rho(\mathbf{k})$ are defined by:

$$\begin{cases} \rho(\mathbf{k}) = -A_c |\mathbf{k}|^2 - |\mathbf{k}|^4 - W(1 - \hat{p}_R(\mathbf{k})) \\ a_{\mathbf{k}} \left[\hat{\phi}_{\mathbf{k}}^n \right] = -|\mathbf{k}|^2 ((3\lambda^2 - 1) \hat{\phi}_{\mathbf{k}}^n - 3\lambda [\hat{\phi}_{\mathbf{k}}^n]^*{}^2 + [\hat{\phi}_{\mathbf{k}}^n]^*{}^3 \\ \quad + |\mathbf{k}|^2 \hat{\phi}_{\mathbf{k}}^n) - W(1 - \hat{p}_R(\mathbf{k})) \hat{\phi}_{\mathbf{k}}^n. \end{cases} \quad (18)$$

Computations were realized on a 1000 × 1000 simulation grid. This way, at least three points were used to describe interfaces for a corresponding 100 nm × 100 nm simulation box in real units at room temperature. The numerical scheme is unconditionally stable. The only criterion for Δt was hence the accuracy of the program for

long time simulations. Δt was set to 0.1 in reduced coordinates (~ 0.01 s at room temperature), associated to a 10^{-3} truncation error.

Simulations were performed using aleatory initial conditions.

IV. RESULTS

A. Parameters computation

To show the potentiality of our model to give a quantitative description of the evolution of a system under irradiation, the microstructure evolution under irradiation in AgCu alloy was modelled. From here, $c(\mathbf{r}, t)$ designates the silver concentration $c_{\text{Ag}}(\mathbf{r}, t)$, and its evolution under irradiation is governed by Eq. (12). Besides, the microstructure consists in silver precipitates in a copper matrix.

1. Equilibrium parameters

a. *Free energy density f_h :* Computing the solubility limits for various temperatures gave the binodal curve presented in Fig. 1 (circle). By construction, it matches the experimental binodal curve (dotted line). This eventually provided us with $a_2(T)$, $a_3(T)$ and $a_4(T)$ (insert of Fig. 1).

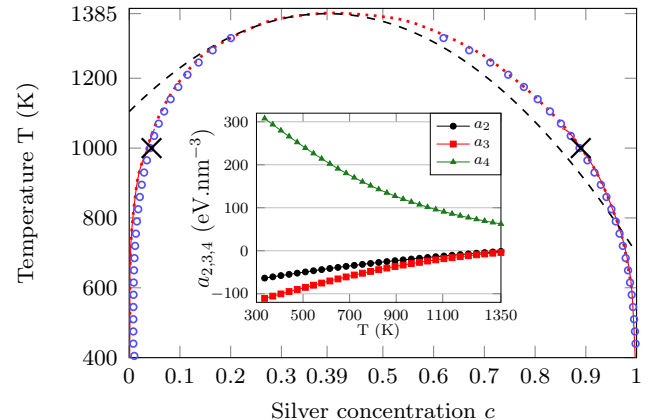


FIG. 1. Experimental phase diagram of silver-copper (dotted line) taken from [42], and comparison with the binodal curve associated to a 2:3:4 potential (present work, circles), and with a standard 2:4 symmetric potential (dashed line). Insert: Landau coefficients a_2 , a_3 and a_4 , defining the free energy density $f_h(c)$, fitted on the experimental phase diagram of silver-copper.

As required by Landau theory, $a_4(T)$ is always strictly positive, while $a_2 < 0$ for $T < T_c$ and cancels for $T = T_c$. At this temperature, the system undergoes a phase transition. For AgCu, it takes place at the critical mean concentration of silver $\bar{c} = c_L = 0.39$ [42]. Consistently with Landau theory, $a_2(T)$ can be approximated by a

linear function close to T_c : $a_2(T) \simeq A(T - T_c)$ [55]. Here, the best linear fit ($\rho = 0.99$) gave $A = 4.8 \times 10^{-2}$ (± 0.05) eV.K $^{-1}$.nm $^{-3}$. As for the cubic term coefficient $a_3(T)$, it is not negligible here, as the system undergoes a first order phase transition when the binodal is crossed. It only cancels at the Landau point (c_L, T_c), where the phase transition becomes of second order. Fig. 1 shows the binodal curve associated to the 2:3:4 potential (circle) intrinsically matches the experimental binodal curve (line). In Fig. 1, we also plotted the binodal curve associated to the standard Landau 2:4 potential from [17, 56] (dashes). Comparison with the experimental curve confirms that the cubic term in our potential is essential to account for the asymmetry of the experimental binodal curve. Indeed, it can be noted that the right branch of the symmetric 2:4 potential displays a strong discrepancy, even for high temperatures, where it is supposed to be most accurate.

b. Interfaces and stiffness parameter κ : The form coefficient of the fitted interface was found to be extremely close to 1, corresponding to the hyperbolic tangent profile. Our fitted interface profile thus intrinsically matched the physical interface given by MC simulations. This correspondence of the fitted (line), and the MC (circles) profiles is illustrated in Fig. 2, at $T = 700$ K.

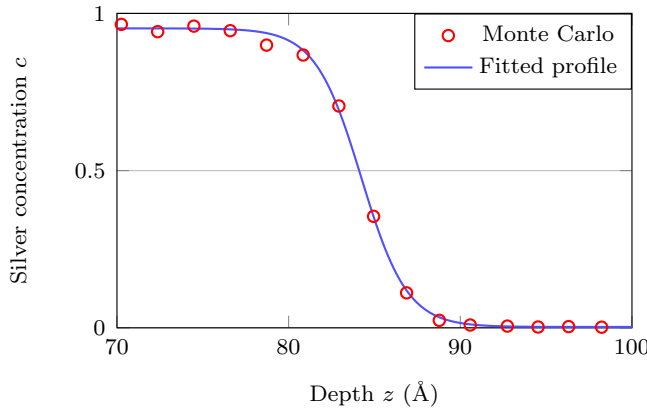


FIG. 2. Silver concentration profile at the interface, determined by our Monte Carlo simulation (circle) for $T = 700$ K, and corresponding phase field profile (line) based on a fit by a Jacobi elliptic sine.

The interface width and the value of κ for different temperatures are gathered in table I. It can be seen that the interface width increases with temperature: from $e = 5.64$ Å at $T = 600$ K, to $e = 7.68$ Å at $T = 900$ K. This range of width is consistent with previous simulations [57]. Besides, the variations of κ remain within the precision uncertainty of our MC simulations, so that κ can be considered constant. From an average over every MC simulation, we could set $\kappa = 0.15$ (± 0.005) eVÅ $^{-1}$. This result seems to deviate from the standard Landau-Ginzburg formalism, where κ is supposed to decrease to 0 as $(T - T_c)^{1/2}$, when T approaches to T_c . Actually, our MC simulations were performed for temperatures up

to 900 K only, so that the corresponding constant value for κ cannot reasonably be transferred above 1000 K, restraining the study to temperatures sensibly inferior to $T_c = 1385$ K. This is actually not much of a restriction, considering that the silver-copper alloy is in liquid phase above 1052 K.

T (K)	e (Å)	κ (eV.Å $^{-1}$)	c_-	c_+	ρ (corr.)
600	5.64 ± 0.01	0.148 ± 0.005	0.004	0.97 ± 0.01	0.9996
700	6.18 ± 0.01	0.146 ± 0.005	0.004	0.96 ± 0.01	0.9997
800	6.84 ± 0.01	0.146 ± 0.005	0.004	0.95 ± 0.01	0.9998
900	7.68 ± 0.01	0.144 ± 0.005	0.009	0.94 ± 0.01	0.9998

TABLE I. Interface width e (Å), and stiffness parameter κ (eV.Å $^{-1}$), from our silver concentration phase field profile, after fitting on our Monte Carlo simulations, and solubility limits c_{\pm} from our Monte Carlo simulations, for various temperatures.

As expected, our atomistic simulations account for the asymmetry of silver solubility limits c_{\pm} . For example, at $T = 900$ K, copper concentration in silver phase is $1 - c_+ = 0.06$, while silver concentration in copper phase is only $c_- = 0.009$.

2. Irradiation parameters

a. Ballistic mixing parameters Γ and R : The preliminary step before computing Γ and R , was the validation of the percolation criterion Eq. (7). In average, we found $L_c = 210$ nm for our cascades, within which $n_{sc} = 6$ subcascades of mean size $l_{sc} \geq 15$ nm were observed. This is consistent with primary knocked atoms (PKA) energies ranging from 80 keV to 180 keV in our simulations [58]. This led to a covering fraction $f_r = 0.4$, thus sufficient to ensure the covering.

It was hence meaningful to display in Fig. 3 the normalized distribution of displacements defined by Eq. (8), for copper (cross) and silver (square) atoms. Obviously, the exponential decay assumption (see Eq. (8)) is validated for both species (best exponential fit: $\rho = 0.97$). However, it is interesting to note the periodically distributed peaks in both distributions. These are actually due to a lower binding energy barrier required for an atom to migrate to a neighbouring site. Besides, the silver and copper atoms distributions are very close. This allowed us to use $R = 3.04$ Å for both species (dashes). This common value of R depends on incident ions species, but not on their initial energy. In our phase field simulations, we used $R = 3.04$ Å for every flux and temperature. This value matches a previous mixed MDrange-molecular dynamics simulation [17] where $R = 3.08$ Å.

The simulations also provided with the total amount of relocated atoms per cascade $N_d = 309000$. Using this result with $L_c = 210$ nm, we could compute the relocation cross section $\sigma^d = 2.01 \times 10^{-13}$ cm 2 . An experimental element of comparison can be found in [59]. For an incident flux $\Phi = 1.21 \times 10^{13}$ cm $^{-2}$ s $^{-1}$ of 1 MeV Krypton

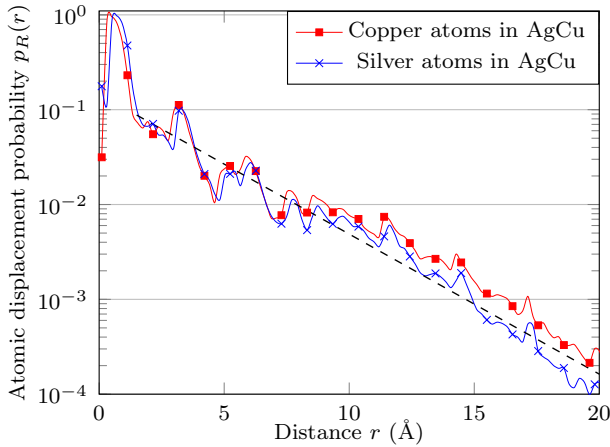


FIG. 3. Normalized distribution of atomic relocation of copper and silver atoms, in polycrystalline $\text{Ag}_{50}\text{Cu}_{50}$ irradiated by Krypton ions of energy 1 MeV, obtained with the BCA code MARLOWE. Average over 1000 trials. Silver and copper distributions display almost equivalent distributions, fitted ($\rho = 0.97$) by a unique exponential distribution of slope $1/R$, $R = 3.04 \text{ \AA}$ (dashes).

ions on polycrystalline AgCu , Enrique and Bellon could measure $\Gamma = 2.8 \text{ s}^{-1}$. Using the same flux, our model shows excellent consistency: $\Gamma = \sigma^d \Phi = 2.53 \text{ s}^{-1}$.

b. *Atomic mobility M under irradiation:* From MARLOWE simulations for 1 MeV Krypton ions, we also extracted the number of Frenkel pairs per cascade before thermal annihilation and sink absorption, $N_V = 19500$. Injecting diffusion numerical data [29–33, 60, 61] in Eq. (5), Eq. (10) and Eq. (B6), we could compute the total mobility for any flux and temperatures. Fig. 4(a) compares the atomic mobility without irradiation (line), and with irradiation, for a flux $\Phi = 10^{13} \text{ cm}^{-2}\text{s}^{-1}$ (triangles).

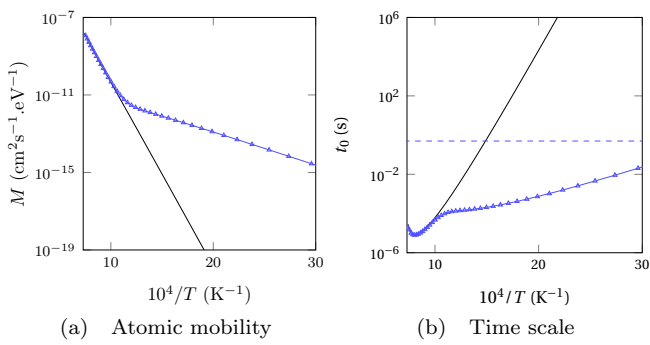


FIG. 4. Atomic mobility (left) and characteristic time scale (right) of silver and copper atoms in AgCu , without irradiation (line), and for $\Phi = 10^{13} \text{ cm}^{-2}\text{s}^{-1}$ (triangle), and time scale of ballistic exchange Γ^{-1} for $\Phi = 10^{13} \text{ cm}^{-2}\text{s}^{-1}$ (dashed line)

The amplitude of M under irradiation matches the thermal mobility for high temperatures ($T > 900 \text{ K}$). Indeed, both follow the same Arrhenius law, and no dif-

fusion enhancement is observed. It can be explained by the saturation of thermal point defects. Yet, a kinking arises when T decreases below 900 K, as the mobility under irradiation becomes by several orders superior to the equilibrium mobility. This observation is of particular matter, as the mobility plays a central part in the characteristic relaxation time of diffusion t_0 (see Eq. (15)). As such, Fig. 4(b) compares t_0 to the characteristic time scale of ballistic relocations in the cascade, $\Gamma^{-1} = 0.498 \text{ s}^{-1}$ (for $\Phi = 10^{13} \text{ cm}^{-2}\text{s}^{-1}$). This allows to investigate the range of temperatures where t_0 and Γ^{-1} are close, so that competition between diffusion effects and ballistic relocations is possible. In the case of equilibrium diffusion (line), this happens above 700 K, versus around 300 K in the present irradiation enhanced mobility model (triangle). This difference will be discussed in section IV.

B. Phase field simulations in reduced coordinates

By the direct observation of the copper precipitates that appeared in our simulations (Fig. 5(a), Fig. 5(b) and Fig. 5(c)) for long times ($t = 10^6$ in reduced time), three evolutions of the microstructure could be distinguished. Each microstructure defines a domain in the (W, R') plane in Fig. 6. $\lambda = 0.25$ and $R' = 2.4$ were set for the 3 microstructure examples displayed in Fig. 5, as they correspond to room temperature in real units, in the case of AgCu under 1 MeV Krypton ions.

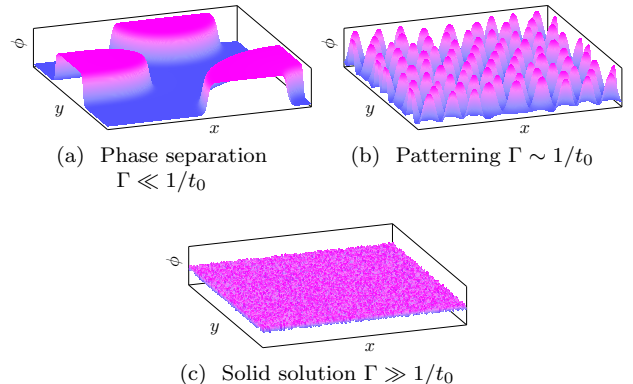


FIG. 5. Reduced concentration ϕ from our phase field simulations: aleatory initial condition with $\bar{\phi} = 0$ ($c(t=0) = c_L$) and $\lambda = 0.25$ ($T < 300 \text{ K}$), on a 1000×1000 mesh grid, with $\Delta t = 0.1$ and $t_{\text{final}} = 10^6$. Top left: demixtion $(W, R') = (0.005, 2.4)$. Top right: patterning $(W, R') = (0.12, 2.4)$. Bottom: solid solution $(W, R') = (1, 2.4)$.

For high values of W (Fig. 5(c), domain (1) in Fig. 6), we observed a homogeneous system corresponding to the formation of a solid solution. In this case, the disordering due to long range displacements induced by irradiation overcomes the expected phase separation driven by thermal diffusion: $\Gamma \gg 1/t_0$. This corresponds to precipitates radius close to 0 at all time. On the contrary, for

small values of W (Fig. 5(a), domain (3) in Fig. 6), diffusion ordering effects are predominant as $\Gamma \ll 1/t_0$. The system displays a macroscopic phase separation, similar to Ostwald ripening [62]. This corresponds to an unbounded growth of precipitates radius. Between these two domains lies the patterning domain (2) (Fig. 5(b)). In this domain, precipitates reach a finite size and remain stationary. This is due to ballistic and diffusional effects coming to equilibrate one another. It is associated to a mean precipitates radius, quickly reaching its finite asymptotic value.

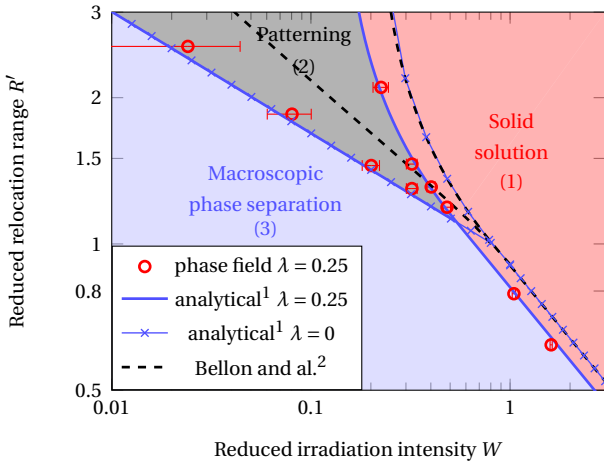


FIG. 6. Phase diagram in reduced coordinates, displaying three microstructure behaviours: solid solution (top right), patterning (top center) and phase separation (bottom left). Comparison between the present phase field study's numerical results (circles) and analytical results¹ from [16] with $\lambda = 0.25$ (thick line), $\lambda = 0.25$ (\times mark), and Bellon and al.'s diagram from [15] (dashed line).

The numerical limits between these three domains (circles in Fig. 6) were determined using two criteria. The first one was the time evolution of precipitates mean size on a sample of 200 solutions, from random initial conditions. The second criterion was the evolution of the Lyapunov function $\mathcal{L}(\phi)$ (see Eq. (16)). Indeed, $\mathcal{L}(\phi)$ converges to a non null limit in the patterning domain, but keeps decreasing in case of macroscopic phase separation, albeit slowly. Numerical limits were superimposed on the three analytical ones from a self-consistent approach [16] (continuous line). Both methods perfectly match. The advantage of our numerical phase field study, is that contrary to the self-consistent analytical work [16], it does not require further simplification such as linearisation of Eq. (14). It should be noted that contrary to chemical disordering, ballistic disordering is of finite range R , and patterning can only be achieved for a sufficient value of R . Indeed, it allows ballistic relocations to display longer range than diffusion migrations ($R \gg l_0$). We also plotted Bellon and al. domain limits based on a spectral method [15] (dashed lines). Though qualitatively similar, the two diagrams quantitatively diverge. This disparity with our results has two origins. First, in

[15], the limit (dashed line) between solid solution (1) and domain formation (2)+(3) differs from ours for $\lambda = 0.25$ (thick line), by a translation operation, due to the use of a symmetric 2:4 potential ($\lambda = 0$ in reduced coordinates). It should be noted that, in the case of AgCu, depending on the temperature, λ varies between 0.15 and 0.25, so it can never be set to 0. This discrepancy emphasizes the necessity for an asymmetric potential based on the experimental phase diagram of AgCu. Second, a mixed tangent-sine ansatz was used in [15] to study the crossing of the demixtion (3)-patterning (2) limit, eventually leading to a smaller patterning domain. Actually, by restraining the concentration profile to particular ansatz in their prospecting for patterned microstructure [15], they missed a variety of patterned microstructure, corresponding to the phase diagram area between the dashed line and the tick line. This can be seen as this limit differs from our estimation at $\lambda = 0$ (\times marks).

C. Phase field simulations in real units: phase diagram under irradiation in (T, Φ) plane

In the case of AgCu irradiated by 1 MeV Krypton incident ions, the reduced diagram in Fig. 6 can be transposed in real units. For that purpose, we used that $R = 3.04 \text{ \AA}$, regardless of Φ and T . As for W , it is fully determined by Φ and T , through $M(\Phi, T)$ (Fig. 4(a)), $a_{2,3,4}(T)$ (insert Fig. 6), $\Gamma(\Phi)$ and κ . This provided us with the phase diagram of silver-copper under irradiation, in the temperature-flux plane displayed in Fig. 7. This result is of great interest, as this diagram can be directly compared to experiments. To our knowledge, no quantitative and predictive study of disrupted coarsening under irradiation had been performed so far, at least in real units.

The three microstructural domains displayed in Fig. 6 are present. The formation of a solid solution of AgCu is achieved for high fluxed and low temperatures (1) where ballistic disordering overcomes diffusion. Complete phase separation (3) occurs for high temperature and moderate fluxes. In these conditions, diffusion ordering effects are predominant. Finally, the patterning domain (2) requires moderate flux and temperature. This allows equilibrium between ion mixing and diffusion. Interestingly, patterning effects can be achieved at room temperature, for realistic fluxes of 1 MeV Krypton ions. This made experimental validation possible.

Wei and Averback [18] performed diffraction experiments on the silver-copper system, irradiated with a $\Phi = 2.5 \times 10^{13} \text{ cm}^{-2}\text{s}^{-1}$ flux of 1 MeV Krypton ions. Their prospecting of eventual steady states were performed for a maximal final dose of $1.9 \times 10^{16} \text{ cm}^{-2}$. Fig. 7 displays excellent consistency between our numerical results (continuous line) and their experiments (cross, triangle and circle).

In details, they observed the formation of a solid solution for $T = 80 \text{ K}$ (triangle), complete separation

of phases for $T = 473$ K (circle), and patterning for $T = 298, 348$ and 398 K (cross). Among these points, the solid solution for $T = 80$ K (liquid nitrogen), the complete separation of phases for $T = 473$ K and the patterning for $T = 348$ K, perfectly match our diagram. Besides the two other patterning points ($T = 298$ K and $T = 398$ K) remain within the uncertainty, notably coming from the choice of migration energies in the atomic mobility in our simulations, as well as the temperature standard deviation of diffraction measures ($\sim \pm 5$ K). Another point corresponding to phase separation is displayed on the diagram: for $T = 423$ K, Wei and Averbach observed an intermediate microstructure between a patterning ($T = 398$ K) and phase separation ($T = 473$ K). They could not conclude whether it was a true steady state or a slow phase separation, as asserted in [15].

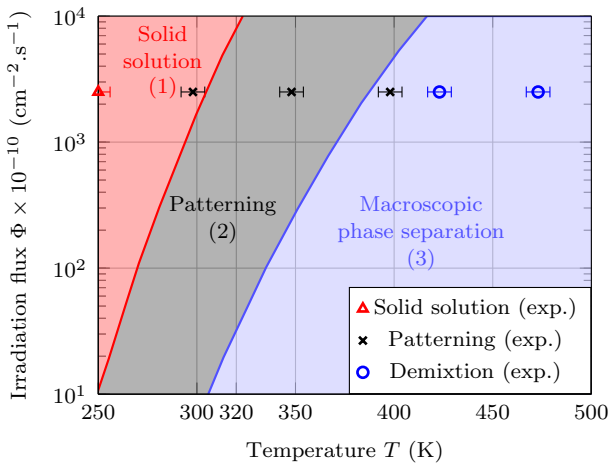


FIG. 7. Phase diagram in the temperature-flux plane for the silver-copper system subjected to Krypton ions (1 MeV) irradiation, displaying three microstructure behaviours: solid solution (top left), patterning (top center) and phase separation (right). For low temperatures and moderate flux, the system displays stationary precipitates (disrupted coarsening). Circle, triangle and cross: diffraction results from Wei and al. [18].

We actually see two reasons why Wei and al. failed to decide whether $T = 423$ K lead to patterning or phase separation. The first one is of experimental nature as discussed in [18]. For this temperature, they could not afford greater dose than $1.9 \times 10^{16} \text{ cm}^{-2}$, as it would lead to experimental artefacts, such as pure copper phase induced by sputtering. Considering this dose was achieved with $\Phi = 2.5 \times 10^{13} \text{ cm}^{-2}\text{s}^{-1}$, the system was followed during 26 minutes top. Still, our study estimated that the characteristic time scale for the microstructure evo-

lution for $T = 423$ K and $\Phi = 5 \times 10^{12} \text{ cm}^{-2}\text{s}^{-1}$ was $t_0 \sim 3 \times 10^{-2} \text{ s}$. Besides, our simulations required at least 10^6 iterations with $\Delta t = 0.1$ ($\times t_0$), viz. almost an hour in real time for the system to reach its final state. 26 minutes was hence barely sufficient to reach the final state in case of phase separation. Moreover, in our study, steady state was always reached within 10^5 iterations in case of patterning. This corresponds to 5 minutes at this temperature. And so, 26 minutes should have been sufficient for the system to reach its steady state otherwise. For that reason, accordingly with [15], this flux-temperature couple leads to phase separation indeed. Second, the limit between patterning and demixing domains is continuous, contrary to the the solid solution-patterning limit. This limit hence rather behaves like an overlapping, suggesting the limit is intrinsically blurred. This makes the distinction between complete phase separation and patterning quite uneasy, whether it is prospected numerically or experimentally.

V. CONCLUSIONS

In this work, the influence of irradiation on steady state patterned microstructures in binary alloys was studied, using a multiscale approach based on phase field. The methodology was applied to the silver-copper system, under Krypton ions irradiation.

First, a phase field model adding an athermal irradiation term [13] based on the ion mixing formalism [35] was set. Contrary to most phase field studies, this model could account for a cubic term in the free energy density. Then, an innovative finite difference scheme [50] was developed, allowing to simulate the late stage microstructure of an irradiated binary alloy in reduced units. Atomistic methods were implemented in parallel, to compute the phenomenological parameters in the case of AgCu irradiated with 1 MeV Krypton ions. Phase field simulations could hence be transferred to real space and time units.

As a result, the temperature and flux leading to patterning in AgCu subjected to 1 MeV Krypton ions was determined. This was summarized in a phase diagram in the flux-temperature plane, which highlighted a patterned microstructure domain, for temperatures ranging from 250 K to 400 K, and incident fluxes greater than $10^{10} \text{ cm}^{-2}\text{s}^{-1}$. This diagram was in excellent agreement with diffraction experiments [18]. To our knowledge, no previous numerical study could achieve this diagram for an irradiated material.

[1] G. Baldinozzi, D. Simeone, D. Gosset, I. Monnet, S. Le Caer, and L. Mazerolles, Phys. Rev. B **74**, 132107 (2006).
[2] A. Harada, , and Q. Tran-Cong*, Macromolecules **30**, 1643 (1997).
[3] G. Schmitz, J. Ewert, F. Harbsmeier, M. Uhrmacher,

and F. Haider, Phys. Rev. B **63**, 224113 (2001).

[4] M. C. Cross and P. C. Hohenberg, Rev. Mod. Phys. **65**, 851 (1993).

[5] H. Bernas, J.-P. Attané, K.-H. Heinig, D. Halley, D. Ravelosona, A. Marty, P. Auric, C. Chappert, and Y. Samson, Phys. Rev. Lett. **91**, 077203 (2003).

[6] Y. Cheng, Mater. Sci. Rep. **45** (1990).

[7] R. Stoller and A. Calder, J. Nucl. Mater. **283**, Part **2**, 746 (2000).

[8] P. Krasnouchtchekov, R. S. Averback, and P. Bellon, Phys. Rev. B **72** (2005).

[9] V. L. Ginzburg and L. D. Landau, Sov. Phys. **20** (1950).

[10] J. W. Cahn, Acta Metall. **9**, 795 (1961).

[11] P. C. Hohenberg and B. I. Halperin, Rev. Mod. Phys. **49**, 435 (1977).

[12] N. Lecoq, H. Zapsolsky, and P. Galenko, DYNAMICAL SYSTEMS, 953 (2011).

[13] G. Martin, Phys. Rev. B **30**, 53 (1984).

[14] R. S. Averback and P. Bellon, Topics in Appl. phys., **116**, 1 (2010).

[15] R. Enrique and P. Bellon, Phys. Rev. Lett. **84**, 2885 (2000).

[16] D. Simeone, G. A. Demange, and L. Lunéville, Phys. Rev. E **88** (2013).

[17] R. A. Enrique, K. Nordlund, R. S. Averback, and P. Bellon, J. Appl. Phys. **93**, 2917 (2003).

[18] L. C. Wei and R. S. Averback, J. Appl. Phys. **81**, 613 (1997).

[19] L.-Q. Chen, Annu. Rev. Mater. Res. **32**, 113 (2002).

[20] P. Tolédano and V. Dmitriev, *Reconstructive phase transitions: in crystals and quasicrystals* (World Scientific, 1996).

[21] M. Hazewinkel, J. F. Kaashoek, and B. Leynse, *Pattern Formation for a One Dimensional Evolution Equation Based on Thoms River Basin Model*. (Springer, 1986).

[22] A. R. Allnatt and A. B. Lidiard, *Atomic transport in solids* (Cambridge University Press, 2003).

[23] L. S. Darken, *Diffusion, Mobility and their Interrelation through Free Energy in Binary Metallic Systems*, Tech. Rep. (1948).

[24] A. J. Bray and C. L. Emmott, Phys. Rev. B **52**, R685 (1995).

[25] A. Ges, O. Fornaro, and H. Palacio, J. Mater. Sci. **32**, 3687 (1997).

[26] G. Martin, Phys. Rev. B **41**, 2279 (1990).

[27] D. B. Butrymowicz, J. R. Manning, and M. E. Read, J. Phys. Chem. Ref. Data (1976).

[28] G. Demange, *Mise en œuvre d'une approche multi-échelles fondée sur le champ de phase pour caractériser la microstructure des matériaux irradiés : application à l'alliage AgCu*, Ph.D. thesis, École Centrale de Paris (2015).

[29] S. M. Foiles and al., Phys. Rev. B **33** (1986).

[30] K. Nordlund and R. Averback, Phys. Rev. Lett. **80**, 4201 (1998).

[31] J. B. Adams, S. M. Foiles, and W. Wolfer, J. Mater. Res. **4** (1988).

[32] P. Wynblatt, J. Phys. Chem. Solids **30**, 2201 (1969).

[33] W. Triftshuser and J. D. McGervey, Appl. phys. **6**, 177 (1975).

[34] D. Simeone, L. Lunéville, and G. Baldinozzi, Phys. Rev. E **82** (2010).

[35] P. Sigmund and A. Gras-Marti, Nucl. Instrum. Methods **182**, Part **1** (1981).

[36] P. Misaelides, *Application of Particle and Laser Beams in Materials Technology* (Springer Science, 1994).

[37] E. Antoshchenkova, L. Lunéville, D. Simeone, R. Stoller, and M. Hayoun, J. Nucl. Mater. **458**, 168 (2015).

[38] R. Sizmann, J. Nucl. Mater. **69**, 386 (1978).

[39] A. Barbu and G. Martin, *Materials under irradiation*.

[40] H. E. Cook, Acta Metall. **18**, 297 (1970).

[41] M. Lavrsky, H. Zapsolsky, and A. Khachaturyan, arXiv preprint arXiv:1411.5587 (2014).

[42] J. L. Murray, I, 261 (1984).

[43] M. Briki, *Étude du couplage entre structure et ordre chimique dans les agrégats bimétalliques: vers l'établissement de diagrammes de phases à l'échelle nanométrique*, Ph.D. thesis, Université Paris Sud-Paris XI (2013).

[44] S. Shao, J. Wang, A. Misra, and R. G. Hoagland, Sci. Rep. **3** (2013).

[45] A. Saxena and A. Bishop, Phys. Rev. A **44**, R2251 (1991).

[46] S. Chee, B. Stumphy, N. Vo, R. Averback, and P. Bellon, Acta Mater. **58**, 4088 (2010).

[47] G. Demange, E. Antoshchenkova, D. Simeone, and Lunéville, to be published (2016).

[48] F. Bokonte, F. Djurabekova, J. Samela, K. Nordlund, S. A. Norris, and M. J. Aziz, Nucl. Instrum. Methods in Physics Research B **297** (2013).

[49] J. Ziegler, Comput. Math. Appl..

[50] D. J. Eyre, , 1 (1998).

[51] B. Vollmayr-Lee and A. Rutenberg, Phys. Rev. E **68**, 066703 (2003).

[52] A. M. Stuart and A. R. Humphries, SIAM rev. **36**, 226 (1994).

[53] L. Song, Y. Zhang, and T. Ma, J. Math. Anal. Appl. **355**, 53 (2009).

[54] X. Ye, Comput. Math. Appl. **44**, 213 (2002).

[55] V. I. Tokar, *Thermodynamics, Microstructures and Plasticity* (Nato Science Series, 2003).

[56] R. A. Enrique and P. Bellon, Phys. Rev. B **63**, 134111 (2001).

[57] P. Wynblatt and S. Dregia, Colloque de physique **51** (1990).

[58] E. Metelkin and A. Ryazanov, At. Energ. **83**, 653 (1997).

[59] R. A. Enrique and P. Bellon, Appl. Phys. Lett. **78** (2001).

[60] A. K. Bandyopadhyay and S. K. Sen, Phys. Status Solidi **519**, 519 (1990).

[61] J. D. McGervey and W. Triftsh, Phys. Lett. **44** (1973).

[62] I. M. Lifshitz, J. Phys. Chem. Solids **19**, 35 (1961).

Appendix A: Expression of κ

Without irradiation, the interface phase field profile is given by the Jacobi elliptic sine [28]:

$$\eta^{(p)}(x) = A^{(p)} \operatorname{sn} \left[\frac{x}{\Delta^{(p)}}, p \right] - \frac{a_3}{3a_4}, \quad (\text{A1})$$

where $p \in]0, 1]$ is the form factor. The amplitude $A^{(p)}$ and the half width $\Delta^{(p)}$ are given by:

$$A^{(p)} = \alpha \sqrt{\frac{2p^2}{1+p^2}}, \quad \Delta^{(p)} = \frac{1}{\sqrt{1+\frac{a_3^2}{3a_4|a_2|}}} \sqrt{1+p^2} \sqrt{\frac{\kappa}{a_2}}. \quad (\text{A2})$$

For long times, $p \rightarrow 1$ and $\text{sn}(\cdot, p)$ becomes an hyperbolic tangent, so that the interface width $e = 2\Delta^{(1)}$ reads:

$$e = \frac{1}{\sqrt{1+\frac{a_3^2}{3a_4|a_2|}}} 2\sqrt{2} \sqrt{\frac{\kappa}{a_2}}. \quad (\text{A3})$$

Appendix B: Expression of the mobility

Without irradiation, Onsager's irreversible process formalism provides with:

$$M(\eta) = \frac{1 - [2(\eta + c_L) - 1]^2}{8k_B T} [(1 - [2(\eta + c_L) - 1]) D_{\text{Cu}}^* + (1 + [2(\eta + c_L) - 1]) D_{\text{Ag}}^*]. \quad (\text{B1})$$

Here, D_{Cu}^* and D_{Ag}^* are the isotopic diffusion coefficients of copper and silver respectively. Under irradiation, $M = \bar{M} + M^{\text{irr}}$. Based on similar diffusion coefficients of silver, copper and silver-copper alloy, and using the fact that for moderate temperatures, mainly vacancies are present at equilibrium, M^{th} reads:

$$M^{\text{th}} \simeq \frac{\bar{c}(1 - \bar{c})}{k_B T} D_{\text{Cu}}^* \simeq \frac{\bar{c}(1 - \bar{c})}{k_B T} c_V^{\text{eq}} D_V(T), \quad (\text{B2})$$

where $D_V(T)$ is the diffusion coefficient of vacancies in copper. This gives:

$$M^{\text{th}}(T) \simeq \frac{\bar{c}(1 - \bar{c})}{k_B T} D_0^V \exp \left[-\frac{H_V^m + H_V^f - T(S_V^m + S_V^f)}{k_B T} \right]. \quad (\text{B3})$$

where c_V^{eq} is the concentration of vacancies at equilibrium. H_V^m , S_V^m , H_V^f , and S_V^f are the enthalpy and entropy of migration and formation of vacancies in copper respectively. As regards M^{irr} , it originates from the vacancies and interstitials δc_V^{irr} and δc_I^{irr} created in the displacement cascade:

$$\begin{cases} \frac{d\delta c_I^{\text{irr}}}{dt} = \sigma^V \Phi - \frac{4\pi R_{\text{cap}}}{V_{\text{at}}} D_I \delta c_I^{\text{irr}} \delta c_V^{\text{irr}} - k^2 D_I \delta c_I^{\text{irr}} \\ \frac{d\delta c_V^{\text{irr}}}{dt} = \sigma^V \Phi - \frac{4\pi R_{\text{cap}}}{V_{\text{at}}} D_I \delta c_I^{\text{irr}} \delta c_V^{\text{irr}} - k^2 D_V \delta c_V^{\text{irr}}. \end{cases} \quad (\text{B4})$$

$\sigma^V \Phi$ is the defects rate production where $\sigma^V = V_{\text{cell}}/N_{\text{cell}} \times N_V/L_c$, $4\pi R_{\text{cap}}/V_{\text{at}} D_I$ is the thermal annihilation rate of point defects, where $R_{\text{cap}} \simeq 2.5a_0$ is the recombination radius of Frenkel pairs in AgCu. $-k^2 D_{V,I} \delta c_{V,I}^{\text{irr}}$ is the sink absorption at precipitates interface, where $1/k$ is the average size of precipitates. Stationary concentrations are thus given by:

$$\delta c_I^* = \sqrt{\frac{\sigma^V \Phi V_{\text{at}}}{4\pi R_{\text{cap}} D_I}} \sqrt{\frac{D_V}{D_I}}, \quad \delta c_V^* = \sqrt{\frac{\sigma^V \Phi V_{\text{at}}}{4\pi R_{\text{cap}} D_I}} \sqrt{\frac{D_I}{D_V}}. \quad (\text{B5})$$

Note the inverse size of precipitates k disappears, which exonerates us from knowing the microstructure, to compute δc_V^{irr} and δc_I^{irr} . We eventually get:

$$M^{\text{irr}} = \frac{2\bar{c}(1 - \bar{c})}{k_B T} \sqrt{\frac{D_0^V \sigma^V V_{\text{at}} \Phi}{4\pi R_{\text{cap}}}} \exp \left[-\frac{H_V^m - T S_V^m}{2k_B T} \right]. \quad (\text{B6})$$